Article

Use of Hidden Markov Model Technique to Characterize and Classify the Wideband Mobile Radio Channel in Different Environments

Rafael S. Azevedo[1], Edson Cataldo[1], Leni J. Matos[1]
[1]*Telecommunications Engineering Department, Fluminense Federal University, Niterói, Rio de Janeiro, Brazil.*
rafaelazevedo@id.uff.br, ecataldo@id.uff.br, lenijm@id.uff.br

***Abstract*— Mobile radio channel and its effects on the radio link path place fundamental limitations on the performance of wireless communication systems. This paper sets out a new approach for wideband modeling of mobile radio channels to classify distinct environments. It applies the hidden Markov model technique to different data sets of the main temporal dispersion parameters of the mobile radio channel: average delay and delay spread. The applied technique has proven to design properly the transitions among those temporal dispersion parameters, mapping statistically the transitions from one point in space to another, and it has revealed to be a feasible option to classify and describe statistically the wideband radio channel in each propagation medium.**

***Index Terms*—** Hidden Markov model, mobile radio channel, time dispersion parameters, swept-frequency technique.

I. INTRODUCTION

Currently, the ecosystem created around mobile communication systems produces huge technological contributions that generate countless direct and indirect jobs and bring numerous improvements in productivity and efficiency. The social and economic impacts are enormous, around 28 million jobs were supported by mobile ecosystem in 2022 [1] and the amount of information crossing networks are achieving exponential growth, since more people take advantage of broadband connectivity at hand, allowing access to information in real-time through digital tools and platforms that permeate the daily lives of citizens. Such exploration of new technologies generates commercial opportunities and potential new markets.

Mobile connectivity continues to be a lifestyle for society, allowing an unexpected and countless number of innovations, with benefits spread through different markets, creating a truly global trend. Over 5.4 billion people globally subscribe to mobile services, and 4.4 billion people make use of mobile internet [1]. In Latin America, the number of subscribers that use mobile internet exceeded 380 million [2]. It is an important step towards keeping people connected, addressing the gap in internet usage, and closing the digital divide.

Considering ongoing progress of wireless communication systems, these high-performance

 © 2024 SBMO/SBMag *ISSN 2179-1074*

systems, generation after generation, have evolved to support a wide range of devices and services to meet the needs of different market segments [3]. Indeed, the radio propagation environment, called mobile radio channel (MRC), places huge and fundamental limitations on the performance of radio communication systems [4]-[5]-[6]-[7], and the adequate ability to predict the propagation of the radio signal in different transmission environments is crucial. Proposals for narrowband and wideband modeling of MRC have become extremely important and aim to be added to the already existing and established physical models of MRC statistical characterization, such as: Saleh-Valenzuela model [8]-[9], which characterizes the dispersive behavior of the indoor radio channel in the time domain through the successive generation of instantaneous responses; autoregressive modeling [10]-[11], that estimates the model parameters from measurements of the channel frequency responses and apply the principle of maximum entropy; the modeling of generation and disappearance of scattered waves [12]-[13], which statistically describes the multipath channel parameters (amplitude, phase, and delay) in the time domain; the stochastic tapped-delay-line (STDL) used to model ultra-wide bandwidth (UWB) indoor channel [14]; and the use of multilayer perceptron (MLP) neural networks for predicting the outdoor-to-indoor coverage [15].

Considering the above, this article comes up with a new proposal that characterizes the wideband MRC in different environments, applying the statistical method of the hidden Markov model (HMM) to the main temporal dispersion parameters of the MRC: average delay and delay spread. It is an extension of the initial works [16]-[17], in which the HMM was used to statistically characterize the indoor-outdoor wideband MRC, producing positive results.

The organization of this paper is as follows: Section II describes succinctly the channel function, HMM application, and the inspiration to present work. Section III briefly details the measurement campaign. Section IV exposes the proposed methodology to apply the HMM. Section V starts by presenting the simulations, and then evaluates the results. Section VI summarizes the ideas discussed throughout the paper, presents the conclusions, and outlines some suggestions for future research.

II. MOBILE RADIO CHANNEL AND HIDDEN MARKOV MODELS

A. Characterization of the mobile radio channel

The electromagnetic waves, here covered by radio waves, propagate through the MRC and they are mainly affected by physical and natural phenomena such as reflection, refraction, scattering, and diffraction [4]. Such phenomena are known as propagation mechanisms [5] and their effects on the radio link path generate multiple waves that propagate through the environment until they reach the destination. The MRC can be a channel mostly with a direct line of sight (LOS) between origin and destination, otherwise it is non-line of sight (NLOS) with several obstacles (mountains, buildings, trees, foliage, cars, pedestrians, etc.) that causes many paths for radio waves and, therefore, this environment is referred as the multipath environment. Thus, the received signal corresponds to the sum of multiple waves with different amplitudes, phases, and delays that propagate along different

received 05 Jul 2023; for review 18 Jul 2023; accepted 29 Feb 2024
© 2024 SBMO/SBMag CC BY
ISSN 2179-1074

paths, multipath propagation, and overlap in the receiving antenna.

The received signals, influenced by the propagation mechanisms along the entire radio link path, present attenuations, and variations in their amplitude. All these signal fluctuations correspond to the phenomenon called fading and, due to its existence, the proper characterization of the MRC takes place following a process divided into two distinct steps: large-scale fading, which includes path loss and shadowing, and small-scale fading, which is concerned with investigating sectors of the order of half a wavelength (λ) [4] and its punctual effects caused by multipath propagation.

MRC controls and limits the performance of the radio communication system. Different channels present constructive and destructive effects, related to propagation mechanisms. Therefore, with the continuous design and progress of mobile communication systems, with evolution in network infrastructure, improvement of mobile devices, and increase the offer of services, an analysis of the MRC must also be developed, since its adequate dimensioning allows more efficient communication.

B. Application of the hidden Markov models

The studies of linked chains of events were conducted initially at the beginning of the 20th century, and they currently present a strong mathematical and tool basis [18]. In many physical, chemical, social, and biological phenomena, among others, the applications of Markov studies are noticed, since these phenomena can be modeled in such a manner that the probability of a current event often depends on the preceding outcome. Many stochastic processes present different degrees of dependence, and Markovian models, or Markovian processes, are special types of stochastic processes that exhibit a simple form of dependence and have applicability regarding the modeling of several phenomena. Therefore, Markov processes are stochastic processes in which the current state is conditionally independent of preceding states given the most recent predecessor state. If Markov processes involve finite, countable, and discrete state space, they are called Markov chains [19].

Although the Markov chains have a wide range of applications, not every phenomenon exposes the respective states directly to the observer. States of the Markov chain are often hidden, and thereby inferences about the phenomenon are only unveiled by examination of secondary incidents. As a result, HMM involves the adoption of two distinct layers (two different stochastic processes), one of them is responsible for representing the unobservable Markov chain, called by hidden states and, similarly, another layer is responsible for exhibiting the secondary incidents that are designated by observable states. The arrows indicate the propagation direction and define the possible connections between states following a probabilistic set of rules, expounding observable states while flowing between hidden states, as illustrated in Fig. 1.

 © 2024 SBMO/SBMag CC BY *ISSN 2179-1074*

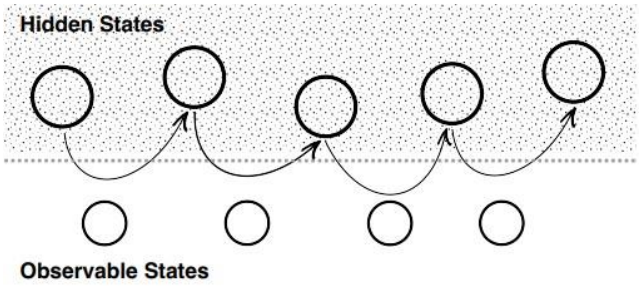

Fig. 1. Hidden states and observable states from HMM technique.

It is worth noting that the layer of hidden states adheres to the Markov property, implying that the current hidden state is conditionally independent of any other preceding hidden state, given its immediate predecessor. Add to this fact that observable states are dependent on the random activity of the hidden states and their results represent the outputs associated with each hidden state or related to each transition between hidden states [20]. Then, the observable states are the sequence of random incidents that directly represent the evolution of the visible stochastic process and, indirectly, the evolution of the hidden stochastic process.

The HMM can be properly applied in dynamic systems modeling [20], ensuring in its random, adaptive, and iterative nature a suitable opportunity for characterizing complex systems, with temporal elements, and even corrupted by other sources and noises [21]. Given this description, HMM can be found in a wide range of signal processing applications, highlighting time-series modeling here, and consequently, this technique was applied in this paper to characterize the MRC and provide a statistical description of its parameters. To this end, each hidden state put together its respective MRC temporal dispersion parameters: average delay (τ_m) and RMS (Root Mean Square) delay spread (σ_T). Each transition between hidden states exhibited its respective observable state, grouping in a two-by-two matrix the MRC parameters τ_m and σ_T of each hidden state. Thus, note that the research focus was on analysis of transitions between hidden states, introducing their particular observable states, and not on antenna receiving power at different reception points in space as previously established by traditional models of MRC characterization. In other words, the major focus was concentrated on analyzing the transitions between states, which is equivalent to analyzing the transitions between the MRC parameters (τ_m and σ_T), trying to design how these temporal dispersion parameters of the MRC transitioned from one point in space to another.

The characterization of MRC applying the HMM method surges as inspiration from the use of the same technique to identify a particular speaker based on a chosen keyword [22]-[23]-[24]. To identify a particular speaker, the HMM method uses database, part for training and another part for testing, to recognize and classify the correct speaker, rejecting any other speaker that have different speech characteristics. Therefore, MRC parameters that describe different environments were investigated. The HMM method used the database of MRC time dispersion parameters, part for training and another part for testing, to recognize and classify properly the transitions between MRC parameters

 © 2024 SBMO/SBMag CC BY *ISSN 2179-1074*

that belong to particular environment, rejecting distinct transitions that describe other environments.

III. MEASUREMENT CAMPAIGN

Firstly, the measurement campaign includes the assembly, calibration, and testing of the necessary equipment. After that, it encompasses the definition and preparation of measurement environments, concluding with the official and definitive measurements.

A. Frequency domain channel sounding and measurement setup

For the wideband MRC characterization in different environments, a channel sounding method in the frequency domain called swept-measurement technique has been adopted, in which 1,601 sinusoidal signal samples of 10 dBm amplitude were generated and transmitted, successively, in discrete frequencies and equally spaced along a frequency band of 750 MHz (from 960 MHz to 1,710 MHz) [25]. The transceiver, vector network analyzer (VNA) equipment, was used through the input port, swept the entire frequency band with the respective 10 dBm sinusoidal carriers and, at the same time, monitored the output port, providing the transfer function of the channel, or channel impulse response, in the frequency domain. It is worth saying that this sounding technique swept-measurement technique is limited to shorter distances because the receiving and transmitting antennas have to be connected to the same VNA equipment [4]. 60-meter coaxial cable was used at the receiving port, permitting to perform measures in distances until that value. The main parameters of the measurement setup are demonstrated in Table I.

TABLE I. CHANNEL SOUNDING PARAMETERS [25]

Parameters	**Value**	**Unit**
Frequency band	960 to 1,710	MHz
Bandwidth	750	MHz
Transmitted power level	+10	dBm
Low Noise Amplifier (LNA) gain	25	dB
Antennas gain	2.14	dBi
Frequency resolution - Δf	0.46875	MHz
Sweep-measuring samples	1,601	-
Sweep-measuring time	696	ms
Delay resolution - $\Delta\tau$	1.333	ns
Maximum delay - τ_{MAX}	2,133	ns

The proper equipment was as follow: VNA (model Hewlett Packard HP8714ET); low noise amplifier (LNA, model MINI-Circuits ZLR-2150); voltage supply 12VCC to energy the LNA; broadband omnidirectional antennas with discone design that were positioned 1.5 m above the ground; laptop to control the measurement campaign and save all measure data; HPIB cable (Hewlett Packard Interface Bus); HP acquisition board to connect the VNA to laptop with Matlab software interface; coaxial cables (models RG-213 and RG-58U) and N-type and SMA-type connectors.

The swept-measurement technique made it possible to measure the proposed environments, since there was a dual relationship between time and frequency domains, and thereby the main temporal

 © 2024 SBMO/SBMag CC BY *ISSN 2179-1074*

dispersion parameters of the MRC in the time domain were provided indirectly via measurements of the channel impulse response in the frequency domain [5]. The system was carefully calibrated through the enhanced calibration functionality, which allowed direct-wired connection between input and output ports using all cables and connectors of the measurement campaign, except the antennas. This direct-wired connection incorporated the propagation losses from the used equipment, enabling the data recorded during the measurement campaign reflected only the behavior of the propagation channel. The enhanced calibration was performed before each measurement to ensure the compensation for equipment losses. Additionally, the transmitter and receiver were synchronized properly, and measurements were collected at several distances.

B. Environments of the measurement campaign

The measurement campaign was performed in two different Campi from Fluminense Federal University (UFF), Praia Vermelha Campus and Gragoatá Campus, both located in Niterói city, Rio de Janeiro, Brazil [25]. The environments were previously selected for the measurement campaign and correspond to so-called indoor, outdoor, and transition environment from internal to external place (indoor-outdoor), or vice versa (outdoor-indoor).

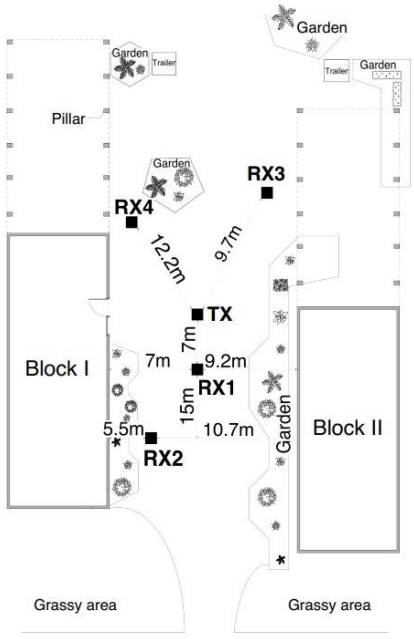

(a) Plant layout of the site 1, UFF Gragoatá Campus.

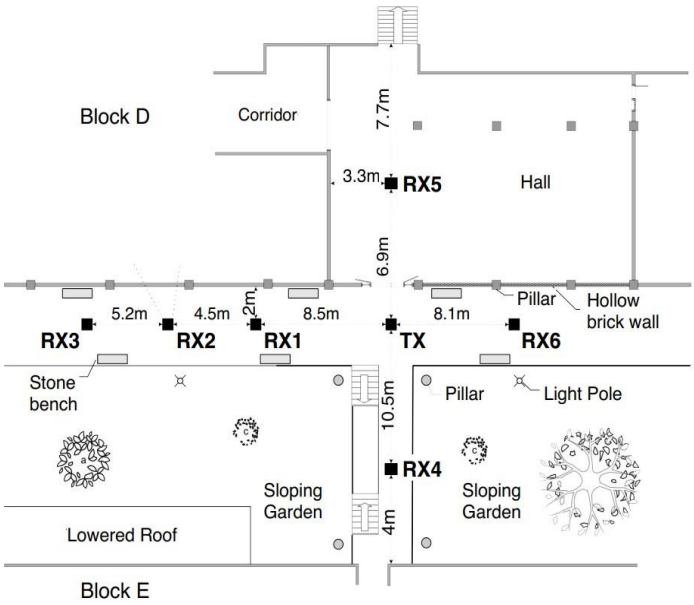

(b) Plant layout of the site 2, UFF Praia Vermelha Campus.

© 2024 SBMO/SBMag CC BY

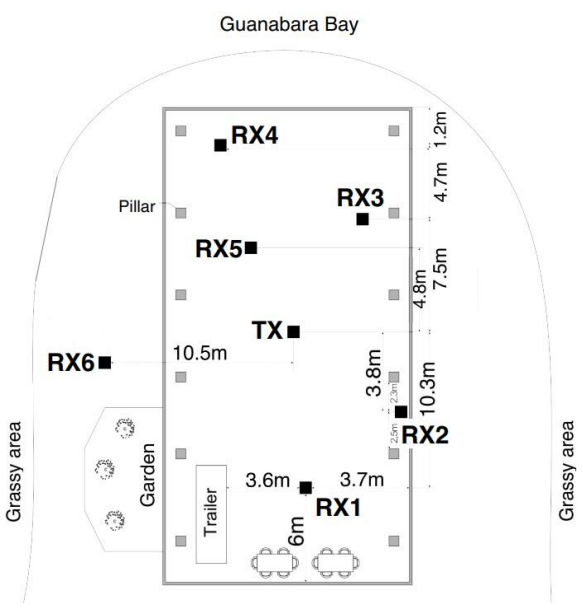

(c) Plant layout of the site 3, UFF Praia Vermelha Campus.

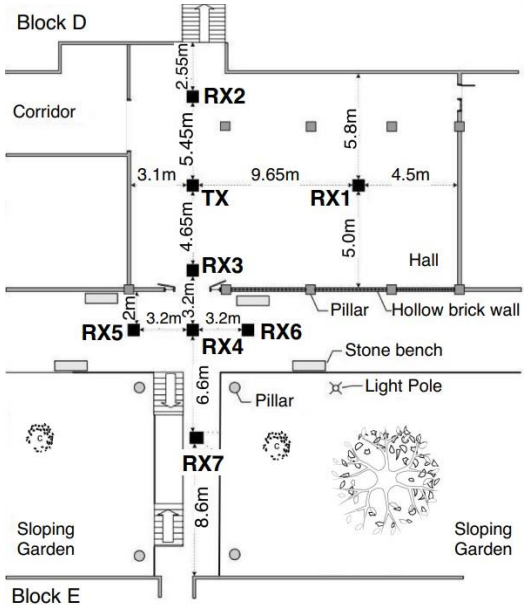

(d) Plant layout of the site 4, UFF Praia Vermelha Campus.

Fig. 2. Plant layout of the measurement campaign environments [25].

Firstly, the measurement campaign was assigned to an external environment, called as site 1, located at Gragoatá Campus. The campaign was performed between blocks I and II, in which parts of both buildings are supported by engaged columns that provide structural support to the buildings with open ground storeys. The site 1 provides a large space that is usual for the movement of people, with the ground-level storey kept free without any construction, except for the columns that transfer the building weight to the ground and stone benches surrounded by gardens and trees. As shown in Fig. 2 (a), reception was set up to capture the channel transfer function at four locations, from RX1 to RX4.

The measurement campaign was conducted in an outdoor-indoor environment, here called site 2, located at Praia Vermelha Campus. The campaign once again was performed between two buildings on the ground floor, in which there is a footpath, surrounded by stone benches, a garden on a sloping area and trees. As illustrated in Fig. 2 (b), the reception was set up to capture the channel transfer function at six locations, most part at the external path along the stone benches, except for RX4 and RX5 which were set up along the footpath linking the buildings and inside the block D, respectively.

The next measurement campaign was organized outdoors, called site 3, located at Praia Vermelha Campus. It was performed on the ground floor, among engaged columns that provide structural support to the building, with open ground storeys and surrounded by garden, low growing vegetation, grassy areas and close to Guanabara Bay. As shown in Fig. 2 (c), the reception was set up to capture the channel transfer function at six locations, from RX1 to RX6, most part under the building.

Finally, the last measurement campaign was conducted in an indoor-outdoor environment, here called site 4, located at Praia Vermelha Campus. Site 4 is a close picture of the last path from site 2. The campaign was performed on the ground floor, starting at a large and open hall into block D and

 © 2024 SBMO/SBMag CC BY *ISSN 2179-1074*

heading towards block E, passing through the footpath that connects the buildings. It is an external path surrounded by stone benches, a garden on a sloping area and trees. As illustrated in Fig. 2 (d), the reception was set up to capture the channel transfer function at seven different locations, part at the hall and part along the external footpath connecting the buildings.

C. Official data collection

Once the equipment was properly inspected and calibrated, the signal reception at positions of all different locations concerned only the propagation channel through which the signals propagated.

At each selected environment, the reception was set up to capture the channel transfer function at different locations, which shall be appointed as RX. For each location RX, a 6-by-6 quadrangular grid was set up, mapping 36 reception dots (positions) equally spaced by 15 cm [16]. Working with wideband frequency, in which the values of λ ranged between 17.54 cm (upper frequency of 1,710 MHz) and 31.25 cm (lower frequency of 960 MHz), given that 0.38 λ is the necessary distance between uncorrelated samples [4], the spacing of 15 cm was calculated to guarantee that the measurements of the 36 dots of each location were not correlated. Hence, the equally spaced dots, set apart by 15 cm in the grid, were sufficient to ensure the de-correlation at signal reception among the 36 dots as shown in Fig. 3.

The measurements of the channel transfer function at each dot were performed in a row, one after the other until reaching the 6-by-6 quadrangular grid at each location RX. During the frequency sweep of 696 ms performed in each dot, a set of 1,601 samples of 10 dBm equally spaced swept the entire 750 MHz bandwidth, thereby generating 1,601 impulse responses that were recorded. This stored database was preprocessed and treated to achieve, in the time domain, a set of 1,601 samples of the channel impulse response. Based on this information, the temporal dispersion parameters of the MRC (τ_m and σ_T) were reached.

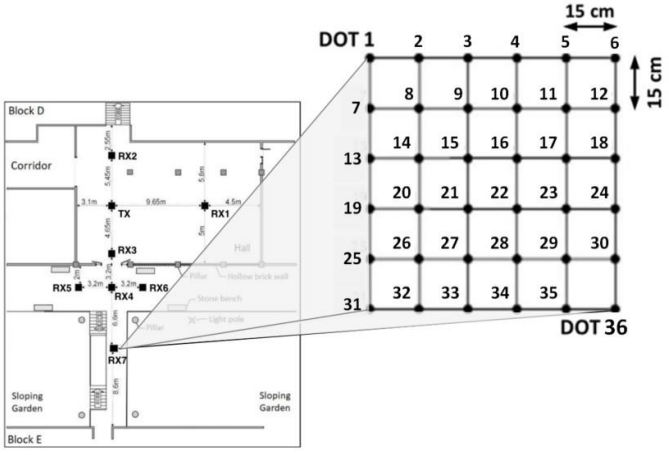

Fig. 3. Map of 6-by-6 quadrangular grid creating 36 reception dots equally spaced by 15 cm at each location RX [16].

It is important to emphasize that during the frequency sweep of 696 ms, which was entirely treated as a time instant, special attention and all necessary precautions were put in place to ensure the MRC

 © 2024 SBMO/SBMag CC BY *ISSN 2179-1074*

remained static. Measurements were carried out during least busy hours (weekends and evening late or early morning) and researchers ensured no movement of people and themselves surrounding the measurement site on the time instant of frequency sweep. Therefore, no changes in the environment were seen during the frequency sweep of 696 ms, guaranteeing an instantaneous measurement.

IV. RESEARCH METHODOLOGY

A. Data acquisition and preprocessing from MRC

A complex phenomenon such as MRC associates the excitation and response signals through the so-called stochastic processes, representing ongoing events over time. Although this observed random response of the MRC occurs with temporal variation, a time-invariant nature may be incorporated by accepting the process as a chain of short events, in which into these short segments the mean received signal strength becomes constant, and main scatters and general characteristics of the current location persist fixed. By taking into account the 36 measurements of impulse response performed in a row as the concatenation of short events [4], in which it is regarded that the variables assume discrete values and the autocorrelations are invariant during short temporal transitions, it is admitted to design each RX as a radio channel named Quasi-Wide-Sense Stationary Uncorrelated Scattering (QWSSUS) [26].

Once the reception captured the channel frequency responses at each dot of the 6-by-6 quadrangular grid in different locations, in which each location was designated as RX, a database of impulse responses for all RX locations was created. It is also certain that MRC remained static during the frequency sweep of the entire 750 MHz or, put simply, during the time interval of 696 ms, which then could be seen as a moment, one point in time for each one of 36 measurements of each location RX.

Therefore, the created database put together received signals at different moments, different points in time, and gathering consecutive measurements of amplitudes and phases of the channel frequency responses. For each moment, each dot (position) in the 6-by-6 quadrangular grid, the data correspond to the responses of the channel through the frequency sweep with sinusoidal carriers and, therefore, relate to the channel transfer function T(f, t) defined as the MRC frequency response for each moment, each point in time [4]. Since the channel is considered a linear filter, the input and output records are characterized directly T(f, t). The 3-term Blackman-Harris window function was used to minimize the spectral leakage, caused by the discretization, and the Inverse Discrete Fourier Transform (IDFT) was applied to obtain the impulsive responses of the channel, $h(t,\tau)$. From them, the power delay profiles $P_h(\tau)$ could be obtained for each one of the 36 measurements of each RX location [4]. In these profiles, the CFAR (Constant False Alarm Rate) technique was applied to clean the noise [16]-[27], highlighting and filtering only valid paths through their amplitudes and delays. After pre-processing these data, the parameters for MRC characterization were obtained: τ_m and σ_T [4]. Thus, for each position of the 6-by-6 quadrangular grid of each measurement RX location, matrices with values of τ_m and σ_T, were generated. These 36 x 2 two-dimensional matrices were

 © 2024 SBMO/SBMag CC BY *ISSN 2179-1074*

called matrices of local characteristics.

B. Bakis topology

An important part of the adopted modeling concerns how HMM hidden states should move along the Markov chain. The choice of a suitable topology for modeling real systems with HMM represents a valuable approach. This is evidenced when thinking about the number of essential iterations and the consequent amount of required processing to train the HMM model. In essence, the freer the topology is, the higher the number of possible paths between states to be covered. For ergodic topology, in which each state can reach any other state, it is plausible to envisage that the number of possible paths increases exponentially with the number of transitions.

Since the practical execution imposes limits on the size of the model [20]-[22], it should be considered, whenever possible, the appropriate restriction on the number of paths to be covered, that is, a balance between flexibility and efficiency for the adopted topology should always be looked for. Because of this, the Bakis topology [20]-[28] was adopted. It is a simplification of the left-to-right topology, allowing only forward transitions, along the permitted states, and leading to an upper triangular transition matrix once it jumps only to later states. It brings greater efficiency to the necessary iterations and training, while maintaining some flexibility, presenting a temporal structure. So, to speak, this topology allows the transition to the subsequent state, the permanence in the current state, or a jump from only one subsequent state, as illustrated in Fig. 4.

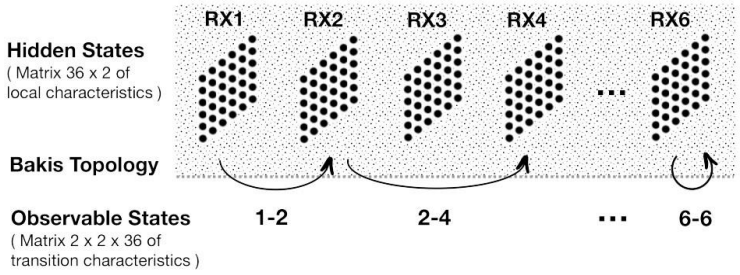

Fig. 4. The adoption of the HMM technique and Bakis topology to characterize the MRC.

C. Characterization of MRC using HMM

The statistical method HMM plays a significant role in dynamic systems modeling [20], as it ensures in its random, adaptive, and iterative nature, an adequate opportunity for characterizing complex systems, with temporal elements and even corrupted by other sources and noises [21]. Therefore, the HMM has been widely adopted by researches in different contexts [16]-[22]-[28]-[29]. Given its robustness, with iterative algorithms that automatically adjust the parameters of the model, the HMM served as the basis for the modeling and analysis of the MRC. Through it, the hidden states (unobservable Markov chain), representing the set of RX locations, put together its respective temporal dispersion parameters (τ_m and σ_T) and the transition between two hidden states (between each RX locations), following the Bakis topology, generated their respective observable states.

After the acquisition of the parameters τ_m and σ_T for each RX location and storage of them in each

 © 2024 SBMO/SBMag CC BY *ISSN 2179-1074*

respective matrix of local characteristics, the complete data of all matrices of local characteristics had to be adapted to the operation of the HMM toolbox for Matlab [30]. As mentioned previously, to fit the data in the HMM toolkit properly, the matrix of local characteristics of each RX location corresponded to the hidden state. The transitions between two hidden states, following the Bakis topology, allowed the grouping of the dispersion parameters, τ_m and σ_T, of the MRC in three-dimensional matrices of the type 2 x 2 x 36, gathering the 36 parameters τ_m and σ_T of each two RX locations randomly. These three-dimensional matrices were named matrices of transition characteristics and, in the context of the HMM, they correspond to the sequence of observable states, the visible stochastic process.

When the matrices of transition characteristics were grouped, indicating the passage from one hidden state to another (passing through different RX states), according to the Bakis topology, the matrix with four dimensions was created and named feature base matrix from MRC. This feature base matrix was divided in half between matrix of training base and matrix of test base. Thus, 50% of the data were used for initialization and training base with the Baum-Welch algorithm [16], while another 50% were used for test base in the following sequence: log-likelihood measurements were obtained for all samples of the matrix of the test base; the outliers (discrepant values) were removed, the data were also split into reference group (25% to calculate the threshold values) and a test group (25% to test the created threshold values).

To train the HMM, regarding the characterization of the MRC, the initialization and training steps were considered. For initialization, scanning processes were performed to discover optimal values. Still in the initialization process, assuming that each state usually generates groups of typically close observables, clustering analyses were performed with the iterative k-means algorithm to gather vectors of similar observables and to associate these vectors with the Gaussian mixtures of states. Furthermore, in the training stage, the Baum-Welch algorithm was used to train and maximize the model parameters. Based on the initial values, the most probable paths were calculated (expectation) and the probabilities were recalculated based on the new paths previously calculated (maximization). This process generated new initial values that were used in place of the old ones. In this way, iterations were created until the calculations reached a stopping criterion, which could be a value of improvement in likelihood compared to the previous parameters, a limited number of iterations, or even a combination of the two previous criteria.

For the matrix of the test base, concerning to the reference group, the data were used to define threshold values. These threshold values corresponded to the log-likelihood values used as references. In other words, for each matrix of transition characteristics, from one state to another, the test group values that are above the analyzed threshold value will be considered valid log-likelihoods. Four different threshold values were defined with which the test groups were compared [16]-[31]. Threshold value descriptions are indicated in Table II.

 © 2024 SBMO/SBMag CC BY *ISSN 2179-1074*

For the matrix of the test base, concerning to the test group, log-likelihood values were used for the estimation of probability density functions, using the ksdensity command of Matlab. Each transition between states created a respective probability density function.

It is important to note that likelihood deals with model adjustments according to a particular data set, or a set of observed incidents. That way, for likelihood, given a set of incidents, the parameters of the probability distribution are adjusted to fit the observed data. Likelihood maximization concerns the adjustments of the probability distribution parameters to maximize the adequacy of this distribution to the observed data.

TABLE II. DETAILS OF THE CHOSEN THRESHOLD VALUES [16]

Threshold values	Description
1. Mean of log-likelihoods	Simple arithmetic mean between the average of the log-likelihoods of the location under analysis and other locations.
2. Cross-mean of values	The average of the log-likelihoods of the location under analysis is multiplied by the standard deviation of the log-likelihoods of the other locations. The average of the log-likelihoods of the other locations is multiplied by the standard deviation of the log-likelihoods of the location under analysis. The simple arithmetic mean of the two values obtained is calculated.
3. Percentile P20 of log-likelihoods	It is the boundary that represents the upper value from the 20th percentile of the log-likelihood data presented.
4. Percentile P20 of p.d.f.	It is the boundary that represents the upper value from the 20th percentile of the probability density functions (p.d.f.)

In practical and even computational terms, it is more appropriate to work with likelihood using the logarithm function because logarithm is a monotonic function, and its maximization is equivalent to the maximization of the function itself. The use of logarithmic simplifies mathematical analysis and computational numerical precision, since the sum of logarithmic probabilities is more favorable than the product of small probabilities [32]-[33].

With both, threshold values and probability density functions based on log-likelihood values, the results were obtained through: Graphical analysis of probability density functions versus threshold values (each graph indicated four calculated threshold values and probability density functions, based on the trained HMM for each respective transition between states) and analysis of the trained HMM models (confusion matrices were used to classify the positioning of the log-likelihoods in relation to the best fit threshold value calculated for each state transition). The above procedure for fitting the HMM to data can be summarized as a pseudocode, as indicated in Table III.

TABLE III. PSEUDOCODE THAT FITS THE HMM TO DATA

Pseudocode	Pseudocode output
1. Calculate τ_m and σ_T for each dot at the 6-by-6 quadrangular grid.	Parameters τ_m and σ_T for each dot at the 6-by-6 quadrangular grid.
2. Create 36 (6-by-6) x 2 (τ_m and σ_T) two-dimensional matrix.	Matrix of local characteristics (hidden state).
3. Define the transition between hidden states.	Transition follows the Bakis topology.
4. For each transition between two hidden states: - Group 2-by-2 randomly the 36 parameters τ_m and σ_T. - Create 2 x 2 x 36 three-dimensional matrix.	Matrix of transition characteristics (observable state).
5. Group all matrices of transition characteristics.	Feature base matrix (four-dimensional)

© 2024 SBMO/SBMag CC BY

6. For feature base matrix: - Create the matrix of training base. - Create the matrix of test base.	Matrix of training base (half of feature base matrix). Matrix of test base (half of feature base matrix).
7. For matrix of training base: - Run HMM initialization and training.	Trained HMM.
8. For matrix of test base: - Calculate log-likelihood values. - Remove the outliers. - For remaining log-likelihood values: - Create the matrix of reference group. - Create the matrix of test group.	Matrix of reference group (half of remaining log-likelihood values). Matrix of test group (half of remaining log-likelihood values).
9. For matrix of reference group: Calculate four different threshold values.	Four different threshold values.
10. For matrix of test group: Calculate the probability density function.	Probability density function (p.d.f.).
11. Calculate the p.d.f. versus threshold values.	Probability density graph.
12. Check which threshold value is the best fit in the identification of valid log-likelihoods.	Best threshold value selected.
13. Calculate the confusion matrix using the best threshold value.	Confusion matrix.

V. SIMULATIONS AND RESULTS

Different simulations have been run to endorse and expand the initial results from [16] and [17], in which the HMM was designed to statistically describe the respective transitions between two states and between more states to characterize the MRC.

As previously described, at each selected RX location, the reception equipment was set up to acquire the impulse response at each dot of 6-by-6 quadrangular grid. The four different sites described in section III have been investigated separately, commonly classified among the options indoor-outdoor, outdoor-indoor, and outdoor. Each site had its number of RX locations (measurement environments) and, given the proposed methodology using Bakis topology, the focus of simulations was concentrated at on the evaluation of hidden states transitions considering different numbers of transitions or, in other words, simulations evaluated the transitions between the temporal dispersion parameters of the MRC by passing through all set of RX locations. For each simulation, several attempts were performed to define the Gaussian mixtures and number of iterations, resulting in optimal values of 2 and 20, respectively.

A. Simulation 1: HMM technique applied to site 1 with 3 transitions between 4 hidden states

Simulation 1 looked closely at a set of 2-by-2 transitions between 4 hidden states from site 1 (outdoor). For that purpose, the Bakis topology generated a set of pre-defined state transitions, establishing in advance how would occur the transitions between the locations from RX1 to RX4. Therefore, 3 transitions between hidden states were defined, allowing only the transition from one to the subsequent hidden state RX, as shown in Fig. 5.

Fig. 5. Bakis topology and the pre-defined state transitions for simulation 1 and simulation 2.

As a result, the matrix of transition characteristics 2 x 2 x 36 was generated for each transition mentioned above, grouping the respective MRC parameters τ_m and σ_T. These 2 x 2 x 36 matrices were

 © 2024 SBMO/SBMag CC BY *ISSN 2179-1074*

put together, indicating the passage through 4 different RX hidden states, forming a feature base matrix of type 2 x 2 x 36 x 3. Half of the samples in the feature base matrix were reserved for HMM training and the other half was used for testing and validation. It should be noted that this division was made for each one of the 3 transitions; therefore, both the training base and the test and validation base grouped data from all transitions. For initialization, a value of 2 was assigned to the number of hidden states, once this simulation was examined each transition individually. Having said that, for half of the samples from the feature base matrix assigned to the test and validation set, the log-likelihood values were calculated, outliers were removed, and the remaining samples were split to create the threshold values and to test the log-likelihood values.

Based on graphical analysis, the transition results between hidden states RX1 to RX2 (1-2), RX2 to RX3 (2-3), and RX3 to RX4 (3-4) can be seen in Fig. 6, Fig. 7, and Fig. 8, respectively. About the transition under analysis and the particular trained HMM, each figure indicates four calculated threshold values and the probability density functions of the three transitions regarding to their log-likelihood values. For each hidden state transition in question, it can be observed that threshold number 3 (percentile P20 of log-likelihoods) is the one with the best fit in the identification of valid log-likelihoods, since the majority part of the probability density function of log-likelihood values are in the right side of threshold number 3 and minority part of values are in the left side of it.

Therefore, the evaluation using the confusion matrix considered only threshold number 3. A total of 3 transitions between 4 hidden states were analyzed, each transition with 36 combinations 2-by-2 of MRC parameters τ_m and σ_T. From each of the 36 combinations, half were used for initialization and training base. Another half, the test base, was used to calculate the log-likelihood measurements of which 2 outliers were removed, and only 16 values remained under review, of whom 8 were used to calculate the threshold values and 8 were used to calculate the probability density function from the respective transition under analysis.

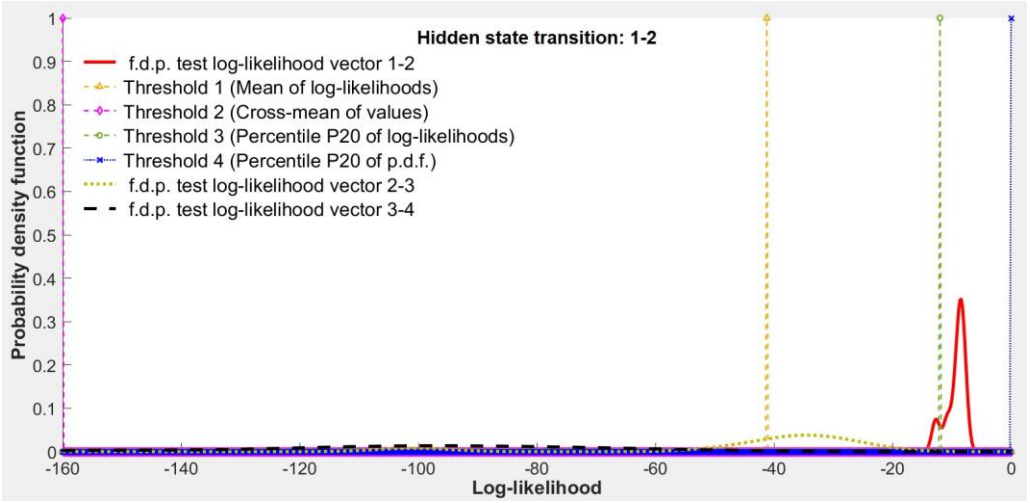

Fig. 6. Results of transitions between hidden states, from RX1 to RX2 (1-2).

© 2024 SBMO/SBMag CC BY

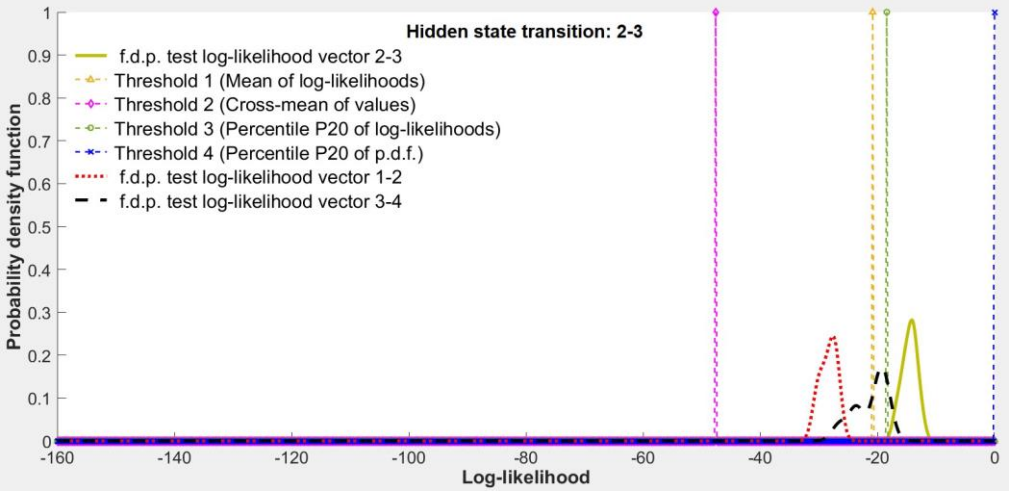

Fig. 7. Results of transitions between hidden states, from RX2 to RX3 (2-3).

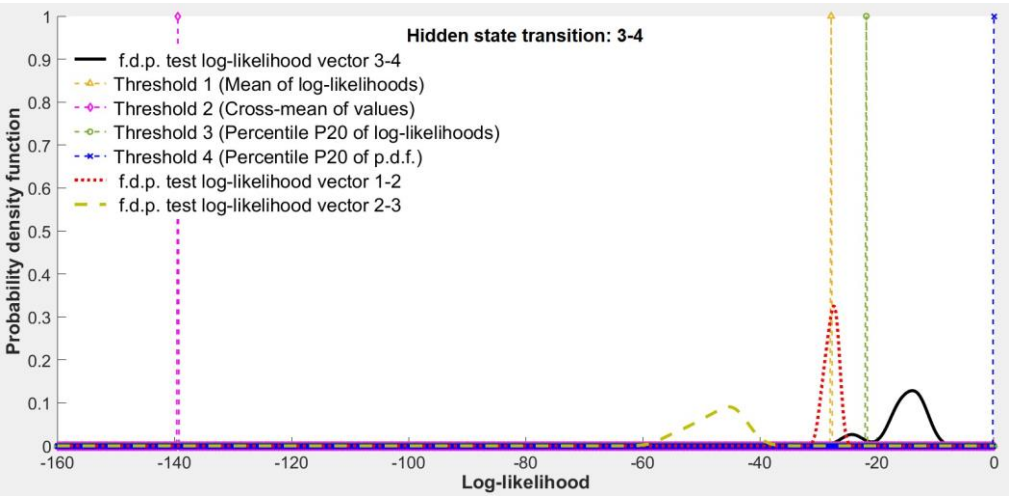

Fig. 8. Results of transitions between hidden states, from RX3 to RX4 (3-4).

Based on that, it can be seen in Table IV that the percentages of the true positive and false negative columns refer only to respective transition under analysis and, true negative and false positive columns correspond to the other 2 transitions of hidden states. As a result, it is possible to observe that HMM hit 7 of 8 log-likelihood values in transition 1-2, 8 of 8 in transition 2-3, and 7 of 8 in transition 3-4. Additionally, the HMM correctly rejected all log-likelihood values from other transitions, discarding 16 of 16 in each transition 1-2, 2-3, and 3-4.

TABLE IV. CONFUSION MATRIX FOR TRANSITIONS SET OF SITE 1

Hidden state transition under analysis	True positive	False negative	True negative	False positive
1-2	87.5% (7/8)	12.5% (1/8)	100.0% (16/16)	0% (0/16)
2-3	100.0% (8/8)	0% (0/8)	100.0% (16/16)	0% (0/16)
3-4	87.5% (7/8)	12.5% (1/8)	100.0% (16/16)	0% (0/16)

© 2024 SBMO/SBMag CC BY

B. Simulation 2: HMM technique applied to site 2 with 3 transitions between 4 hidden states

Simulation 2 examined the set of 2-by-2 transitions between 4 hidden states from site 1 (outdoor) as a whole, rather than examining each transition one by one as indicated in simulation 1. Then, the Bakis topology generated the same set of pre-defined state transitions, as shown in Fig. 5.

The matrix of transition characteristics 2 x 2 x 36 was generated for each one of the 3 transitions between 4 four hidden states, grouping τ_m and σ_T, and forming a feature base matrix of type 2 x 2 x 36 x 3. Half of the samples of the feature base matrix were reserved for HMM training and the other half was used for testing and validation. It should be noted that this division was made for each transition, so that both the training base and the test and validation base grouped data from all transitions. For initialization, a value of 4 was assigned to the number of hidden states, once this simulation was examining the whole set of 3 transitions.

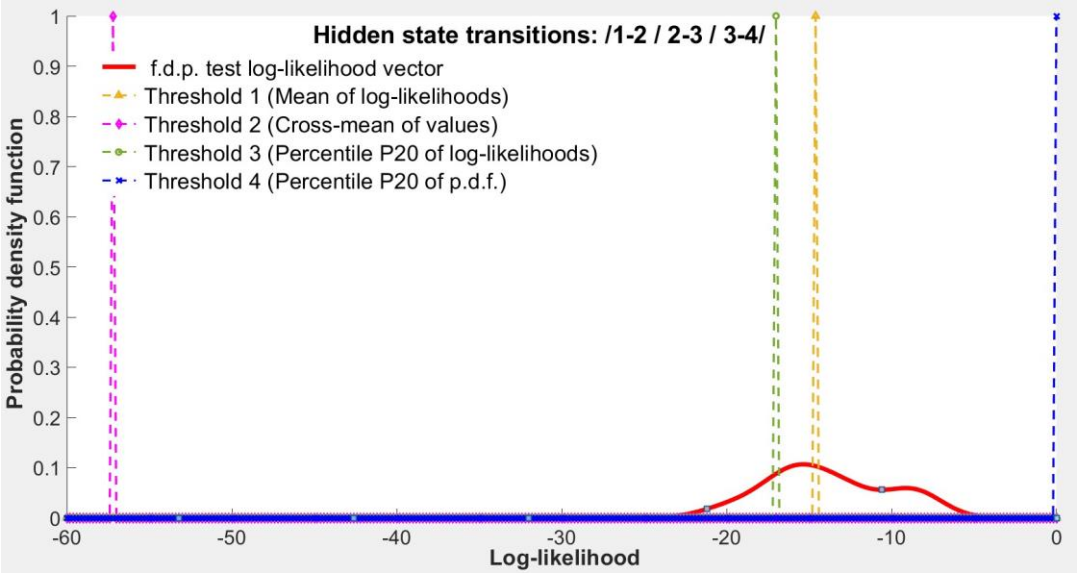

Fig. 9. Results of 3 transitions between 4 hidden states from site 2.

That said, for half of the samples from the feature base matrix assigned to the test and validation set, the log-likelihood values were calculated, outliers were removed, and the remaining samples were split to create the threshold values and to test the log-likelihood values. The results based on graphical analysis are shown in Fig. 9. The red line is about the probability density function based on log-likelihood values, considering the total set of 3 transitions between hidden states. It can be seen that threshold number 3 (percentile P20 of log-likelihoods) is still the threshold with the best fit in valid log-likelihoods identification.

In addition, since the analysis was carried out with the entire feature base matrix (total set of 3 transitions between hidden states), for the analysis using the confusion matrix, there were no data for the true negative and false positive columns. Considering only threshold number 3, it was possible to set up the confusion matrix seen in Table V. The HMM succeeded in hitting 22 (84.6%) of 26 tested log-likelihood values. Therefore, erroneously rejected 4 (15.4%) tested values.

© 2024 SBMO/SBMag CC BY
ISSN 2179-1074

TABLE V. CONFUSION MATRIX FOR ALL TRANSITIONS SET OF SITE 1

Hidden state transition	True positive	False negative	True negative	False positive
1-2 / 2-3 / 3-4	84.6% (22/26)	15.4% (4/26)	0% (0/0)	0% (0/0)

C. Simulation 3: HMM technique applied to site 2 with 8 transitions between 6 hidden states

As initially applied to simulation 2 (outdoor site), simulation 3 in turn followed the same steps to examine an outdoor-indoor site, exploring the set of 2-by-2 transitions between 6 hidden states from site 2. Thus, the Bakis topology generated 8 pre-defined state transitions as seen Fig. 10.

The matrix of transition characteristics 2 x 2 x 36 was generated for each one of the 8 transitions between 6 hidden states, grouping τ_m and σ_T, and forming a feature base matrix of type 2 x 2 x 36 x 8.

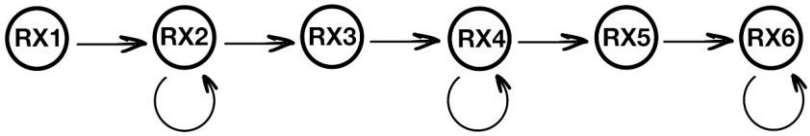

Fig. 10. Bakis topology and the pre-defined states transitions for simulation 3 and simulation 4.

As in the previous simulation, half of the samples of the feature base matrix was reserved for HMM training, another half was used for testing and validation, and a value of 9 was pointed to the number of hidden states. From samples assigned to the test and validation set, the log-likelihood values were calculated, outliers were removed, and the remaining samples were split to create the threshold values and to test the log-likelihood values.

The results based on graphical analysis are indicated in Fig. 11. The red line is about the probability density function based on log-likelihood values, considering the total set of 8 transitions between hidden states. It can be seen that threshold number 3 (percentile P20 of log-likelihoods) is still the threshold with the best fit in valid log-likelihoods identification.

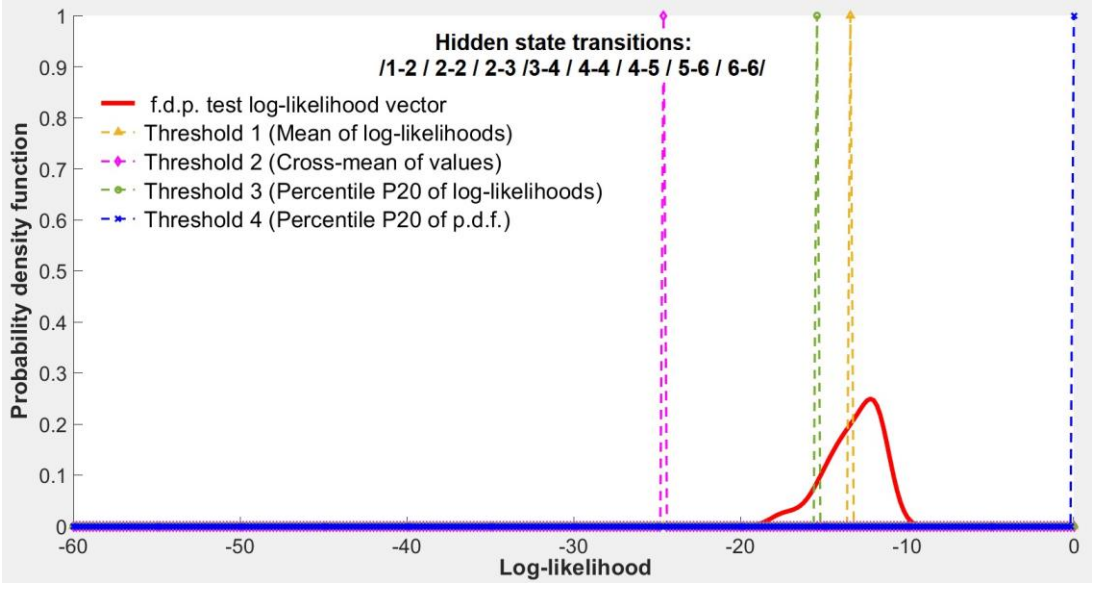

Fig. 11. Results of 8 transitions between 6 hidden states from site 2.

© 2024 SBMO/SBMag CC BY

Taking into account only threshold 3 and the fact that there were no data for the true negative and false positive columns, the confusion matrix was created, and it can be viewed in Table VI. The HMM succeeded in hitting 64 (91.4%) of 70 tested log-likelihood values. Therefore, erroneously rejected 6 (8.6%) tested values.

TABLE VI. CONFUSION MATRIX FOR ALL TRANSITIONS SET OF SITE 2

Hidden state transition	True positive	False negative	True negative	False positive
1-2 / 2-2 / 2-3 / 3-4 / 4-4 / 4-5 / 5-6 / 6-6	91.4% (64/70)	8.6% (6/70)	0% (0/0)	0% (0/0)

D. Simulation 4: HMM technique applied to site 3 with 8 transitions between 6 hidden states

As previously applied in simulation 2 (outdoor site) and 3 (outdoor-indoor), simulation 4 inspected in detail an outdoor site, investigating the set of transitions between 6 hidden states from site 3 (outdoor). Therefore, the Bakis topology generated 8 pre-defined state transitions as shown in Fig. 10.

Each of the 8 transitions between 6 hidden states created its own matrix of transition characteristics 2 x 2 x 36, combining τ_m and σ_T to create a feature base matrix of type 2 x 2 x 36 x 8.

Samples of the feature base matrix were divided, half for training and half for testing and validation of the HMM. Just as before, a value of 9 was assigned to the number of hidden states. For the test and validation set, the log-likelihood values were computed, outliers were deleted, and the remaining samples were moved apart to create and test the threshold values.

Once again, the red line is related to the probability density function based on log-likelihood values while taking into consideration the total set of 8 transitions between hidden states. The threshold number 3 (percentile P20 of log-likelihoods) is still the one with the best fit in valid log-likelihood identification. The results based on graphical analysis can be seen in Fig. 12.

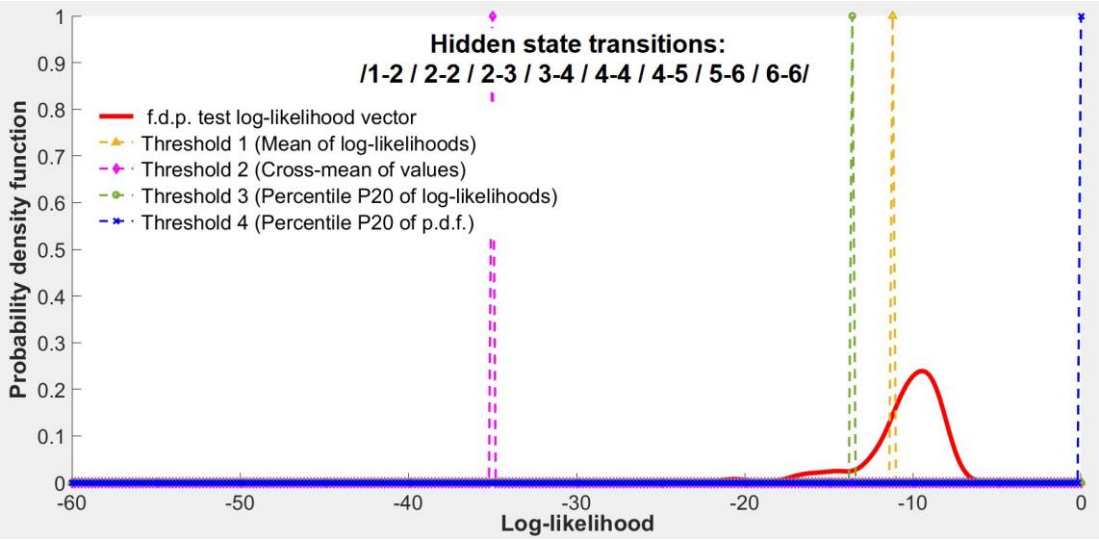

Fig. 12. Results of 8 transitions between 6 hidden states from site 3.

Considering threshold 3 and knowing that there were no data for the true negative and false positive columns, the confusion matrix was created, and it can be visualized in Table VII. The HMM succeeded in hitting 63 (90.0%) of 70 tested log-likelihood values. Therefore, erroneously rejected 7

 © 2024 SBMO/SBMag CC BY

(10.0%) tested values.

TABLE VII. CONFUSION MATRIX FOR ALL TRANSITIONS SET OF SITE 3

Hidden state transition	True positive	False negative	True negative	False positive
1-2 / 2-2 / 2-3 / 3-4 / 4-4 / 4-5 / 5-6 / 6-6	90.0% (63/70)	10.0% (7/70)	0% (0/0)	0% (0/0)

E. Simulation 5: HMM technique applied to site 4 with 9 transitions between 7 hidden states

Just as in simulation 4 (outdoor site), simulation 5 followed the same route to explore in turn the set of transitions between 7 hidden states from site 4 (indoor-outdoor) as a whole. To this end, the Bakis topology generated a set of pre-defined state transitions, establishing in advance how would occur the transitions between the locations from RX1 to RX7. Thus, 9 transitions between hidden states were defined, as seen in Fig. 13.

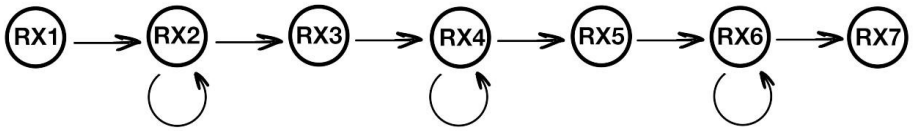

Fig. 13. Bakis topology and the pre-defined states transitions for simulation 5.

As a result, the matrix of transition characteristics 2 x 2 x 36 was generated for each of the 9 transitions mentioned above, grouping the respective MRC parameters τ_m and σ_T. These 2 x 2 x 36 matrices were put together, indicating the passage through different RX hidden states, forming a feature base matrix of type 2 x 2 x 36 x 9. Half of the samples of the feature base matrix was reserved for HMM training and the other half was used for testing and validation. It should be noted that this division was made for each one of the 9 transitions, so that both the training base and the test and validation base grouped data from all transitions. For initialization, a value of 10 was assigned to the number of hidden states. That said, for half of the samples from the feature base matrix assigned to the test and validation set, the log-likelihood values were calculated, outliers were removed, and the remaining samples were split to create the threshold values and to test the log-likelihood values.

Based on graphical analysis, the results can be seen in Fig. 14. The red line corresponds to the probability density function based on log-likelihood values, considering the total set of 9 transitions between hidden states. It can be observed that threshold number 3 (percentile P20 of log-likelihoods) is again the one with the best fit in the identification of valid log-likelihoods, since the majority part of the probability density function of log-likelihood values are in the right side of threshold number 3 and minority part of values are in the left side of it.

© 2024 SBMO/SBMag CC BY
ISSN 2179-1074

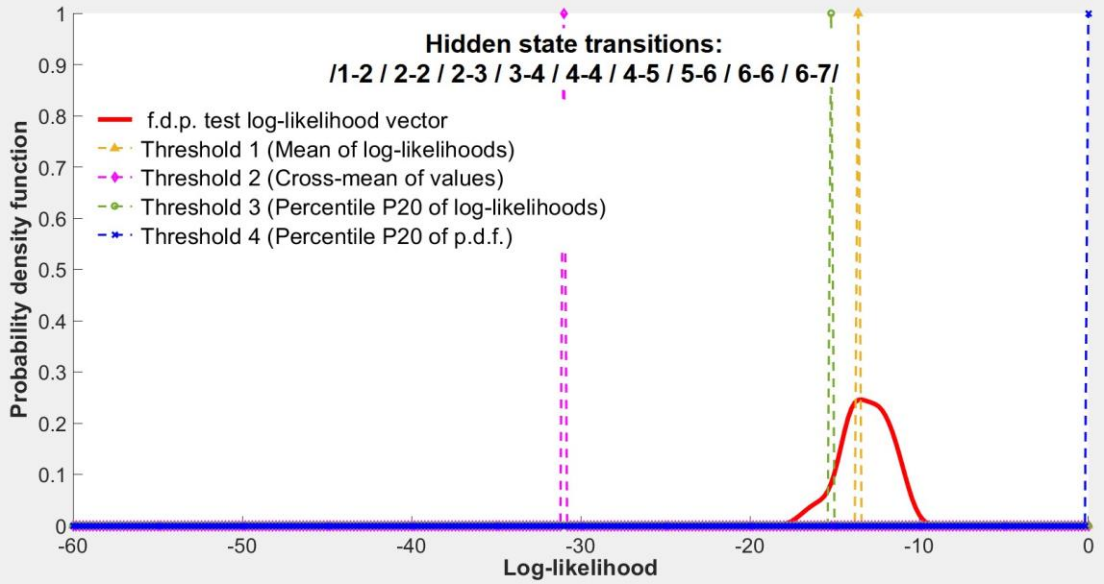

Fig. 14. Results of 9 transitions between 7 hidden states from site 4.

In addition, since the analysis was carried out with the entire feature base matrix (total set of 9 transitions between hidden states), for the analysis using the confusion matrix, there were no data for the true negative and false positive columns. Considering only threshold number 3, it was possible to set up the confusion matrix seen in Table VIII. The HMM succeeded in hitting 73 (92.4%) of 79 tested log-likelihood values and, therefore, it erroneously rejected only 6 (7.6%) tested values.

TABLE VIII. CONFUSION MATRIX FOR ALL TRANSITIONS SET OF SITE 4

Hidden state transition	True positive	False negative	True negative	False positive
1-2 / 2-2 / 2-3 3-4 / 4-4 / 4-5 5-6 / 6-6 / 6-7	92.4% (73/79)	7.6% (6/79)	0% (0/0)	0% (0/0)

VI. CONCLUSIONS

In the face of the continuous evolution of wireless communication systems, advances in technology have emerged to meet the rapidly growing demand around the world for high-quality mobile services. The progress of these systems encompasses improvements to access goods and services that create a cycle of productivity gain and new opportunities.

Under the above technological breakthroughs, once the MRC imposes major restrictions on the high-performance of wireless communication systems, this paper brought forward innovation since it used the HMM technique and main temporal dispersion parameters of the propagation channel (τ_m and σ_T) to characterize the MRC at different environments (outdoor, outdoor-indoor, and indoor-outdoor) and classify via confusion matrix if data set under analysis belonged or not to environment that was being investigated at each simulation.

The HMM technique was used to examine the transitions between hidden states using the time dispersion parameters τ_m and σ_T and, indeed, it succeeded in hitting in most simulations scores close to or higher than 90%, showing that the HMM technique is a feasible option to describe statistically

© 2024 SBMO/SBMag CC BY
ISSN 2179-1074

the MRC in different environments. It is important to emphasize that all of the focus was set on the evaluation of hidden state transitions, which is equivalent to analyzing the transitions between the MRC parameters, trying to design how these temporal dispersion parameters transitioned from one hidden states to another and the HMM technique was successful on it.

Once the current mobile communication systems make use of multiple antennas, different technologies that work together, and spectral aggregations by combining dynamically different frequency bands, it is becoming increasingly important to consider approaches to characterizing the MRC that do not restrict the adopted parameters to certain ranges of values. In this context, the HMM technique proved to be initially effective in characterizing the MRC and classifying different environments with different amounts of data (different numbers of transitions between hidden states). Through its random, adaptive, and iterative nature, the HMM provided an appropriate and secure opportunity to characterize the MRC. Thus, it is possible to go ahead, continue and extended this work with new results as the definition of a model to characterize the MRC or even use this technique as a classification system that identifies when user equipment, such as cell phones, change or handover from one environment to another.

ACKNOWLEDGMENT

The authors thank the National Council for Scientific and Technological Development (CNPq, Brazil).

REFERENCES

[1] GSMA, "The Mobile Economy 2023", *GSMA Intelligence*, 2023. https://www.gsma.com/mobileeconomy/.
[2] GSMA, "The Mobile Economy Latin America 2022", *GSMA Intelligence*, 2022. https://www.gsma.com/mobileeconomy/latam/.
[3] 3GPP "Release 15", Technical Report (TR) 21.915 V15.0.0, 2019. https://www.3gpp.org/specifications-technologies/releases/release-15.
[4] J. D. Parsons, "The mobile radio propagation channel", 2nd ed., John Wiley & Sons Inc., 2000.
[5] T. S. Rappaport, "Wireless communications principles and practice". 2nd ed., Prentice Hall Professional Technical Reference, 2002.
[6] L. G. Ribeiro, L. J. Matos, P. V. G. Castellanos, M. B. Moura, V. L. G. Mota, and W. D. T. Meza, "Influence of vegetation on the outdoor-to-indoor mobile radio propagation in 700 MHz band", *Journal of Microwaves, Optoelectronics and Electromagnetic Applications*, vol. 18, pp. 427-438, 2019.
[7] P. A. Pinna, A. L. Santos, L. J. Matos, P. V. G. Castellanos, F. J. Oliveira, and G. L. Siqueira, "Spatial diversity effect on the experimental gain of capacity of the outdoor mobile radio channel in the 700 MHz band", *Journal of Microwaves, Optoelectronics and Electromagnetic Applications*, vol. 19 (2), 2020.
[8] A. A. M. Saleh and R. A. Valenzuela, "A statistical model for indoor multipath propagation", *IEEE Journal on Select. Areas in Communications*, vol. 5, pp. 128–137, 1987.
[9] F. V. S. Coelho, E. Cataldo, and L. J. Matos, "Simulation of indoor-outdoor and outdoor-indoor radio channel in 960-1700 MHz Band", *IEEE Latin America Transactions*, vol. 15, pp. 1400-1406, 2017.
[10] S. Horward and K. Pahlavan, "Autoregressive modeling of wide-band indoor radio propagation", *IEEE Transaction on Communications*, vol. 40, pp. 1540-1552, 1992.
[11] F. A. L. Silva, L. J. Matos, and E. Cataldo, "Modelo auto-regressivo aplicado a um canal rádio de banda ultralarga", 2008 XVI Brazilian Telecommunications Symposium (SBrT'08), Rio de Janeiro, Brazil, 2008.
[12] H. Iwai and Y. Karasawa, "Wideband propagation model for the analysis of the effect of the multipath fading on the near-far problem in CDMA mobile radio systems", *IEICE, Trans. Comm.*, vol. E 76-B, pp. 103-112, 1993.
[13] R. V. S. Almeida and L. J. Matos, "Emprego da técnica de geração e desaparecimento de raios na simulação de canal UWB em ambiente indoor", 2009 XXVII Brazilian Telecommunications Symposium (SBrT'09), Blumenau, Brazil, 2009.

received 05 Jul 2023; for review 18 Jul 2023; accepted 29 Feb 2024
© 2024 SBMO/SBMag CC BY
ISSN 2179-1074

[14] D. Cassioli, M.Z. Win, and A.F. Molisch, "The ultra-wide bandwidth indoor channel: from statistical model to simulations", *IEEE Journal on Select. Areas in Communications*, vol. 20 (6), pp. 1247-1257, 2002.
[15] M. B. Moura, D. C. Vidal, C. Schueler, L. J. Matos, and T. N. Ferreira, "Outdoor-to-indoor power prediction for 768 MHz wireless mobile transmission using multilayer perceptron", 2018 IEEE World Congress on Computational Intelligence, Rio de Janeiro, Brazil, 2018, Proceedings - International Joint Conference on Neural Networks (IJCNN), vol. 1. pp. 1258-1264, 2018.
[16] L. G. Ribeiro, L. J. Matos, and E. Cataldo, "Aplicação de modelos ocultos de Markov na modelagem do canal rádio móvel", 2020 MOMAG, 19th Brazilian Symposium of Microwave and Optoelectronics (SBMO) and 14th Brazilian Congress of Electromagnetism (CBMAG), Niterói, Brazil, vol. 1, pp. 296-300, 2021.
[17] R. S. Azevedo, L. J. Matos, and E. Cataldo, "Aplicação dos modelos ocultos de Markov na caracterização banda larga do canal rádio indoor", 2022 XL Brazilian Telecommunications Symposium (SBrT'22), Santa Rita do Sapucaí, Brazil, 2022.
[18] U. C. Merzbach and C. B. Boyer, A history of mathematics, 3rd ed., John Wiley & Sons Inc., 2011.
[19] A. Leon-Garcia, Probability, statistics, and random processes for electrical engineering, 3rd ed., Pearson Education Inc., 2008.
[20] J. P. Coelho, T. M. Pinho, and J. Boaventura-Cunha, Hidden Markov models: theory and implementation using Matlab®, CRC Press Inc., 2019.
[21] A. B. Poritz, "Hidden Markov model: a guided tour", *Porc. of the IEEE Int. Conf. on in Acoustics, Speech, and Signal Processing*, pp. 7- 13, 1988.
[22] L. R. Rabiner, "A tutorial on HMM and select app in speech recognition", *Proceedings of the IEEE*, vol. 77, n. 2, 1989.
[23] F. M. Silveira, C. Schueler, and E. Cataldo, "Utilização da técnica MFCC em conjunto com os parâmetros extraídos do sinal glotal para melhorar o desempenho de um sistema de verificação de locutor", 2017 XXXV Brazilian Telecommunications Symposium (SBrT'17), São Pedro, Brazil, 2017.
[24] L. Mendoza, E. Cataldo, M. Vellasco, M. Silva, and J. Apolinario, "Classification of vocal aging using parameters extracted from the glottal signal", *Journal of Voice*, vol. 28, pp. 532-537, 1999.
[25] C. F. Souza, "Análise da dispersão temporal de canais de banda ultralarga (UWB) através de medidas realizadas em ambientes internos e externos", M.S. thesis, College of Eng., Fluminense Federal Univ., Niterói, 2006. https://www.ppgeet.uff.br/site/wp-content/uploads/2021/01/Christiano_Freitas_De_Souza.pdf.
[26] D. Cox, "910 MHz urban mobile radio propagation: multipath characteristics in New York city", *IEEE Transactions on Communications*, 1973.
[27] L. J. Matos and B. S. Marinho, "A comparison of the delay spread obtained with different power delay profiles de-noising techniques", *Engevista*, vol. 13, n. 2, pp. 129-133, 2011.
[28] F. Jelinek, "Continuous speech recognition by statistical methods", *Proceedings of the IEEE*, vol. 64, pp. 532-556, 1976.
[29] F. J. S. Campos, Modelos ocultos de Markov: del reconocimiento de voz a la música, Granada Univ., 2007.
[30] M. Chen, MATLAB central file exchange, hidden Markov model toolbox (HMM), 2023, https://www.mathworks.com/matlabcentral/fileexchange/55866-hidden-markov-model-toolbox-hmm.
[31] S. H. Chen and Y. R. Luo, "Speaker verification using MFCC and support vector machine", 2009 International Multiconference of Engineers and Computer Scientist (IMECS), Hong Kong, 2009.
[32] C. M. Bishop, Pattern recognition and machine learning, Springer, 2006.
[33] S. Haykin, Neural networks and learning machines, 3rd ed., Prentice Hall Professional, 2009.

received 05 Jul 2023; for review 18 Jul 2023; accepted 29 Feb 2024
© 2024 SBMO/SBMag CC BY
ISSN 2179-1074